NJC

ROYAL SOCIETY OF CHEMISTRY

PAPER

View Article Online
View Journal | View Issue

Cite this: *New J. Chem.*, 2024, **48**, 8534

A boron nitride–carbon composite derived from ammonia borane and ZIF-8 with promises for the adsorption of carbon dioxide†

Carlos A. Castilla-Martinez, * Christophe Charmette, Jim Cartier and Umit B. Demirci

In the present study, we report the synthesis, characterization and assessment of the carbon dioxide adsorption capacity of a composite made of boron nitride and carbon. The material is obtained through a two-step process. In the initial step, ammonia borane is introduced into the pores of a zeolitic imidazolate framework (ZIF-8) using a novel one-pot synthesis method. The ZIF-8 is formed *in situ* around the ammonia borane molecules, eliminating the need for an infiltration step. The successful confinement of ammonia borane within the ZIF-8 structure is verified through different characterization techniques (IR, XRD, TGA-DSC, and ^{11}B MAS NMR). In the second step, ZIF-8 containing confined ammonia borane is pyrolyzed. Ammonia borane acts as a precursor of boron nitride and the process results in a composite comprising carbon, boron and nitrogen. The composite was subsequently characterized and evaluated as a potential adsorbent for carbon dioxide. With a specific surface area of 56 $m^2\ g^{-1}$, the composite demonstrates a CO_2 uptake of 1.94 mmol g^{-1} (or 85.4 mg g^{-1}) when exposed to 1.5 bar of CO_2 at 30 °C. This value surpasses reported capacities of other boron nitride-based materials as CO_2 adsorbents. When comparing the CO_2 adsorption capacity in terms of the specific surface area, a significant enhancement is observed (34×10^{-3} mmol m^{-2}). This suggests that the material provides more active sites for CO_2 adsorption, such as polarized B–C, B–N, and C–N bonds. This key factor may be even more important than having a large specific surface area. Therefore, the potential for developing new boron-based materials with enhanced CO_2 adsorption capacities lies in increasing both specific surface area and active sites.

Received 6th February 2024,
Accepted 11th April 2024

DOI: 10.1039/d4nj00643g

rsc.li/njc

1. Introduction

Climate change is acknowledged as an anthropogenic phenomenon that has various impacts on the planet, including the increase of the sea level, ocean acidification, and increased water and air temperatures.[1] All these effects have adverse consequences on ecosystems and humanity. The emission of greenhouse gases into the atmosphere, particularly carbon dioxide (CO_2), is the primary cause of anthropogenic climate change. Thus, one of the humanity's significant challenges is to control CO_2 emissions and mitigate global warming. Carbon capture and storage technologies (CCS) emerge as potential solutions to reduce the concentration of CO_2 in the atmosphere. The fundamental idea is to capture CO_2 before its release and then store it in a secure location to minimize its environmental impact.[2] According to the International Energy Agency, the anticipated CO_2 capture capacity in the energy sector is 0.8 Gt by 2030, 5.6 Gt by 2050 and 10.4 Gt by 2070. Additionally, achieving a net zero-emission of CO_2 by 2070 is a goal.[3]

Different approaches exist for capturing CO_2. For instance, amine scrubbing is one of the most developed technologies for the chemical capture of post-combustion CO_2. However, it poses challenges in terms of the overall cost and energy efficiency.[4] Another promising approach is the capture of CO_2 by porous solids using physical interactions. Various porous materials, such as carbon, silica, metal organic frameworks (MOFs), and polymers, have been considered for physisorption of CO_2.[5–9] Carbon-based materials have shown promising CO_2 adsorption capacities. For example, a carbon doped with sulfur is able to adsorb 3.64 mmol $CO_2\ g^{-1}$ (160 mg $CO_2\ g^{-1}$) at 25 °C and 1 bar of CO_2; nitrogen-rich carbon polymers have exhibited an adsorption capacity of 4 mmol $CO_2\ g^{-1}$ (180 mg $CO_2\ g^{-1}$).[10,11]

Institut Européen des Membranes, IEM – UMR 5635, Univ Montpellier, ENSCM, CNRS, Montpellier, France. E-mail: ccastilla90@gmail.com, carlos.castilla-martinez@umontpellier.fr

† Electronic supplementary information (ESI) available. See DOI: https://doi.org/10.1039/d4nj00643g

Boron nitride (BN) is a material that has recently gained attention as a potential adsorbent for CO_2. BN, analogous to graphite, possesses properties like high mechanical resistance, chemical and thermal stability, and electrical insulation.[12] Experimental studies indicate that BN can adsorb CO_2 under room conditions. Marchesini *et al.* obtained porous BN (1016 $m^2\ g^{-1}$) from urea and boric acid, which was exposed to a CO_2 atmosphere (1 bar, 25 °C) and it showed an adsorption of about 0.6 mmol $CO_2\ g^{-1}$ (26 mg $CO_2\ g^{-1}$).[13] Jiang *et al.* prepared porous BN foam (130 $m^2\ g^{-1}$) starting from ammonia borane and thiourea at 1200 °C. The foam was able to uptake about 0.36 mmol $CO_2\ g^{-1}$ (15 mg $CO_2\ g^{-1}$) under 10 bar CO_2 and at 24 °C.[14] While BN exhibits the capability to adsorb CO_2 under room conditions, these values are not particularly noteworthy when compared to other materials. For instance, reported values for polymer-derived carbons fall in the range of 2.9–3.3 mmol $CO_2\ g^{-1}$ (127–145 mg $CO_2\ g^{-1}$) at 1 bar CO_2 and 25 °C.[15] To enhance the performance of BN-based CO_2 adsorbents, various approaches have been explored. For example, it seems that a high density of ultra-micropores can favor the adsorption and selectivity of CO_2. Gou *et al.* produced porous BN fibers in pellet form (1098 $m^2\ g^{-1}$) from boric acid and melamine.[16] This material, rich in ultra-micropores, was able to adsorb 2.26 mmol $CO_2\ g^{-1}$ (99 mg $CO_2\ g^{-1}$) under 1 bar CO_2 and at 25 °C, with a selectivity of 20.6 with respect to N_2. Another method to improve the CO_2 adsorption capacity is to functionalize the BN structure with different elements. Liang *et al.* introduced Cu into the structure of porous BN nanofibers.[17] The undoped BN nanofibers (715 $m^2\ g^{-1}$) were capable of adsorbing 1.34 mmol $CO_2\ g^{-1}$ (59 mg $CO_2\ g^{-1}$), whereas the Cu-loaded BN nanofibers (653 $m^2\ g^{-1}$) adsorbed 2.77 mmol $CO_2\ g^{-1}$ (122 mg $CO_2\ g^{-1}$). This improvement was attributed to the incorporation of Cu, which altered the electron transfer between the BN nanofibers and CO_2, favoring gas adsorption. Another example was reported by Chen *et al.*, who doped a BN structure with carbon.[18] The porous BCN material (727 $m^2\ g^{-1}$) exhibited CO_2 adsorption values comparable to carbon structures, surpassing those of BN-based materials. Under 1 bar CO_2 and at 25 °C, the BCN material was capable of taking up 3.91 mmol $CO_2\ g^{-1}$ (or 172 mg $CO_2\ g^{-1}$). The incorporation of C atoms into the BN structure increased ultra-microporosity and defects in the material, promoting CO_2 adsorption.

The objective of this study was to synthesize and characterize a material based on carbon, boron and nitrogen with the capacity to adsorb CO_2 under room conditions. By combining BN with carbon, we aimed to improve the adsorption capacity of the material. Ammonia borane (AB) was selected as a precursor for BN, and zeolitic imidazolate framework 8 (ZIF-8), a highly stable material, was chosen as the carbon source. We developed a novel and original synthetic approach to confine AB inside ZIF-8 through a one-step method to obtain the AB@ZIF-8 composite: ZIF-8 was constructed *in situ* around the AB molecules, trapping them inside the ZIF-8 framework. The resulting material was then transformed into a BN/carbon composite (BN@C) through pyrolysis at 800 °C. The material was characterized, and its CO_2 adsorption capacity was evaluated. BN@C exhibited a notable CO_2 capture capacity per specific surface area (1.52 mg $CO_2\ m^{-2}$ or 3.4×10^{-2} mmol $CO_2\ m^{-2}$) likely due to the presence of a high number of active sites, such as the presence of polarized B–C/B–N bonds. The results are presented and discussed in the following sections.

2. Experimental

2.1 Reagents

Zinc nitrate hexahydrate ZnN ($Zn(NO_3)_2{\cdot}6H_2O$, Alfa Aesar, 98%), 2-methylimidazole mIM ($C_4H_6N_2$, Sigma-Aldrich, 99%) and methanol MeOH (CH_3OH, Sigma-Aldrich, anhydrous, 99.8%) were used for the synthesis of the zeolitic imidazolate framework ZIF-8. Commercial ammonia borane AB (NH_3BH_3, Sigma-Aldrich, 97%) was used as received.

2.2 Synthesis of AB@ZIF-8

All syntheses were conducted within an argon-filled glovebox (MBraun M200B; $H_2O \leq 0.1$ ppm, $O_2 \leq 0.1$ ppm; temperature 26 °C). A novel one-pot synthesis was developed, starting with the synthesis of ZIF-8 using a reported route.[19] The ZnN:mIM:MeOH ratio was kept at 1 : 4 : 20 (mmol : mmol : mL). The concentration of AB in the solution was set at 0.5 mol L^{-1}, following the infiltration routes of AB in MOFs as previously reported.[20–22] The objective was to form ZIF-8 around the AB molecules, thereby confining them within the pores of the MOF.

Inside the glovebox, 0.3 g of ZnN was added to 10 mL of MeOH and stirred for 30 min until a clear solution was obtained (designated as solution A). Concurrently, 0.33 g of mIM and 0.32 g of AB were dissolved in 10 mL of MeOH and stirred for 30 min (designated as solution B). Solution B was then slowly poured into solution A, and the mixture was stirred for 24 h. A white suspension was obtained, which was subsequently centrifuged at 6000 rpm for 20 min. The solid was separated from the liquid and dried for 24 h under dynamic vacuum without further washing, and the resulting white powder, denoted as AB@ZIF-8, was recovered and stored in the glovebox for further characterization. For comparison, the synthesis of ZIF-8 was carried out without the presence of AB, following the same procedure.

2.3 The composite BN@C

AB@ZIF-8 underwent pyrolysis in a Vectar Ltd VTF7 tubular furnace at 800 °C, a temperature choice based on a previous study which revealed that bulk BN obtained from AB could adsorb CO_2 when pyrolyzed between 600 and 800 °C.[23]

Prior to the pyrolysis process, the furnace underwent a 30 min vacuum and was then filled with N_2. The sample, AB@ZIF-8, was transferred under an Ar atmosphere to the furnace, and introduced under a flow of N_2 (100 mL min^{-1}). The AB@ZIF-8 composite was heated with a ramp of 1 °C min^{-1}, maintained at 800 °C for 2 h, and then cooled down to room temperature. Subsequently, the resulting composite BN@C was

recovered and stored inside the glovebox. For comparison of CO_2 adsorption properties, a similar heat treatment was applied to pristine ZIF-8, resulting in a carbon-derived from the MOF (referred to as C800 henceforth).

2.3 Characterization

The samples were characterized by different techniques, including N_2 sorption using a Micromeritics TriFlex apparatus (the specific surface area, pore volume, and average pore width were calculated by the Brunauer–Emmett–Teller BET and the Barrett, Joyner and Halenda BJH methods), scanning electron microscopy (SEM) (Hitachi S4800, 15 kV), transmission electron microscopy (TEM) (JEOL 2200 FS microscope, 200 kV, equipped with a STEM-EDX module), Fourier transformed infrared (FTIR) spectroscopy (NEXUS instrument, Thermo Fisher equipped with an attenuated total reflection accessory from 600 to 4000 cm^{-1} wavenumber), magic angle spinning nuclear magnetic resonance (MAS NMR) (^{11}B nucleus, Varian VNMR400, 128.3 MHz), powder X-ray diffraction (PXRD) (PANalytical X'Pert Pro Multipurpose, Cu-$K_{\alpha1/\alpha2}$ radiation λ = 1.5418 Å, 45 kV, 30 mA), thermogravimetric analysis (TGA) (SDT Q600, TA Instruments, under a N_2 flow of 100 mL min^{-1}), and X-ray photoelectron spectroscopy (XPS) (ESCALAB 250 instrument, Thermo Fisher, Al-K_α monochromatized source of 1486.6 eV). The density of the samples was estimated using a Micromeritics AccuPyc II 1345 helium pycnometer at 25 °C. Elemental quantification analyses were carried out to determine the composition of the material. The C, N and H elements were quantified using an Elementar Vario MICRO Cube and the B and Zn elements were quantified by the ICP-OES technique with a PerkinElmer 7000DV instrument. BN@C was digested in a mixture of sulfuric and nitric acids to perform the ICP-OES analysis.

The CO_2 adsorption capacity of the materials was measured in a laboratory-made Sievert device at 30 °C and under 1.5 bar of CO_2. To calculate the isosteric enthalpy of adsorption of BN@C, experiments were carried out under different conditions (temperatures of 10 °C and 45 °C exposed to 1.5 bar and 2.5 bar CO_2). The enthalpy was determined by the Clausius–Clapeyron equation. Prior to the measurements, the samples were degassed at 150 °C under vacuum overnight. Throughout the measurements, the pressure and temperature were monitored with the assistance of a laboratory-made software. The samples were exposed to the CO_2 atmosphere until equilibrium was reached (within 180 min in all cases), and the experiments were conducted two times for reproducibility. The quantity adsorbed by the samples was calculated, considering CO_2 as an ideal gas.

3. Results and discussion

3.1 Textural properties and morphology

The textural properties of the materials are presented in Table 1. Due to the reported dehydrogenation of confined AB at room temperature,[24] specific surface area (SSA) measurements for the AB@ZIF-8 composite were not feasible, as preparing the sample for analysis involves degassing under heating. This would lead to the dehydrogenation of AB. Pristine ZIF-8 exhibited the highest SSA at 1281 $m^2\ g^{-1}$, followed by C800 with 658 $m^2\ g^{-1}$, and finally, the BN@C composite with 56 $m^2\ g^{-1}$. All materials showed a type IV N_2 adsorption isotherm with a hysteresis loop H_4, the characteristic of mesoporous materials (Fig. S1, ESI†). The heat treatment at 800 °C resulted in a reduction in the SSA for the C800 material, suggesting partial shrinking and deformation due to the elevated temperature.[25] The SSA of BN@C was significantly reduced, indicating successful filling of ZIF-8 pores by AB, which then transformed into bulk BN during pyrolysis within the framework.

Table 1 Textural properties of the samples (SSA is the specific surface area and ρ is the density)

Sample	SSA ($m^2\ g^{-1}$)	ρ ($g\ mL^{-1}$)
ZIF-8	1281	0.661
C800	658	0.420
BN@C	56	0.511

SEM analysis was conducted on all samples, while BN@C underwent additional TEM analysis (Fig. 1). All samples present a uniform hexagonal-shaped structure. Based on SEM images, the average particle size values of ZIF-8, AB@ZIF-8 and BN@C were estimated to be 108, 188 and 156 nm, respectively. The incorporation of AB into the solution of ZnN and mIm has no discernible effect on the morphology of the MOF particles (Fig. 1b). Even after the 800 °C heat treatment, the BN@C composite retained a well-defined structure, similar to pristine ZIF-8. This is supported by TEM images (Fig. 1e and f). The STEM-EDX analysis of the BN@C composite confirmed the homogeneous presence of B, C, N, and Zn elements (Fig. S2, ESI†).

3.2 AB@ZIF-8

AB@ZIF-8 was characterized by different techniques. For purposes of comparison, the pristine ZIF-8 was also compared when relevant. IR analyses were carried out, and the spectra of the pristine ZIF-8, AB@ZIF-8 and commercial AB are presented in Fig. 2a. ZIF-8 presents the characteristic bands that are consistent with other studies.[26,27] The bands observed between 2900 and 3100 cm^{-1} are attributed to the C–H stretching vibrational mode, while the bending C–H mode is present between 1200 and 1500 cm^{-1}. Both regions correspond to the aromatic and aliphatic C–H of the imidazole.[28] The band centered at 1580 cm^{-1} corresponds to the stretching mode of the C=N bond in the ZIF-8 structure.

The spectrum of AB shows all the expected vibrational modes.[29] The stretching modes of the N–H and B–H bonds are present at 3100–3500 cm^{-1} and 2100–2500 cm^{-1}, respectively. The N–H bending bands can be seen between 1300 and 1700 cm^{-1}. In the case of the ZIF-8@AB composite, the spectrum is comparable to that of pure ZIF-8. However, a small band appeared at *ca.* 3300 cm^{-1}, indicating the presence of the N–H bonds of AB. In a similar way, low intense bands can be

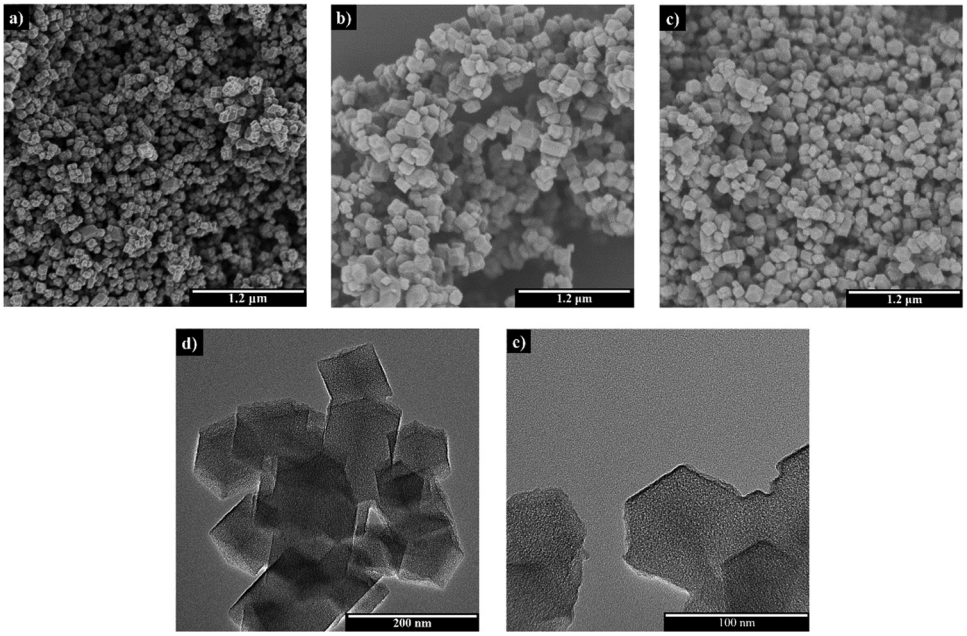

Fig. 1 SEM images of (a) ZIF-8, (b) AB@ZIF-8, and (c) BN@C. TEM images of the BN@C composite with scales of (d) 200 nm and (e) 100 nm.

seen between 2100 and 2500 cm^{-1}, which belong to the B–H bonds. These bands are not present in the pristine ZIF-8, which indicates the presence of AB within the ZIF-8 structure.

The AB@ZIF-8 composite was analyzed by ^{11}B MAS NMR (Fig. 2b). Typically, AB presents a double horn-shaped signal centered at −26 ppm (Fig. S3, ESI†). AB@ZIF-8 presents two signals in the tetra-coordinated boron zone of the spectrum (ppm < 0). The signal at −25 ppm is assigned to the $N\mathbf{B}H_3$ environment of AB. This signal has lost the double horned shape of pristine AB, and other signals have appeared, likely due to the effect of the nanoconfinement.[30] The signal at −17 ppm is attributed to a $N_2\mathbf{B}H_2$ environment, suggesting that borane has undergone dehydrocoupling and it formed polyaminoborane ($-[H_2N-BH_2]_n-$). The absence of a signal between −35 and −45 ppm (typical of BH4 environments) allows us to exclude the presence of the diammoniate of diborane [(NH3)2BH2]+$[BH4]^-$, an ionic dimer formed during the thermolysis of AB.[31] In the tri-coordinated boron region (ppm > 0), two signals are observed, one at 0.7 ppm and another low-intense broad signal between 5 and 15 ppm. These signals are assigned to borate compounds with $\mathbf{B}O_4$ and $\mathbf{B}O_3$ environments. The formation of B–O bonds has been reported when a metal organic framework is used as the scaffold for AB.[32,33] Besides, the use of a solvent like methanol, and the presence of water molecules in the precursors of ZIF-8 ($Zn(NO_3)_2{\cdot}6H_2O$, for instance) may favor the formation of these kinds of bonds (by the occurrence of methanolysis or hydrolysis).

Depending on the scaffold, confined AB behaves in different ways. For example, nanoconfined AB in an activated carbon is not stable over time and it slowly releases H_2, leading to the formation of PAB and other polymeric compounds.[24] To study the stability of the AB@ZIF-8 composite, we stored one sample for 7 months inside the glovebox and after this time, it was analyzed by FTIR spectroscopy and ^{11}B MAS NMR (Fig. S4a, ESI†). On the one hand, the IR spectra showed a slight change in the B–H stretching mode of the compound, where the bands of the aged sample are broader and more pronounced. On the other hand, more pronounced changes were observed by ^{11}B MAS NMR. The signals assigned to the $N\mathbf{B}H_3$ environment nearly disappeared, while the intensity of the signals of the $N_2\mathbf{B}H_2$ environment increased. The presence of a new signal centered at −8 ppm, which is assigned to a $N_3\mathbf{B}H$ environment, suggests the evolution of the sample and the formation of dehydrogenated polymeric residues of AB, such as a branched polyaminoborane. The other signals at positive chemical shifts have broadened and increased in intensity, indicating the formation of $N_2\mathbf{B}H$ environments, implying the dehydrocoupling of the confined AB. Thus, the confined AB is slowly dehydrogenated over time in ZIF-8 (Fig. S4b, ESI†).

ZIF-8, AB@ZIF-8 and pristine AB were also analyzed by PXRD. The patterns of these materials and a reference one of ZIF-8 are presented in Fig. 3.[34] ZIF-8 crystallizes in a body centered cubic unit cell with an *I-43m* space group, and our pristine ZIF-8 exhibits good agreement with the pattern reported in the literature. The diffraction pattern of AB@ZIF-8 is also similar to the reference one. The peaks belonging to AB are not observed and this indicates that AB was successfully trapped inside the MOF structure.[22] The diffraction peaks of the composite have broadened compared to those of pristine ZIF-8, indicating a smaller crystallite size of the particles. The crystallite size was calculated from the XRD patterns by the Scherrer equation, obtaining values of 44.5 nm for ZIF-8 and 28.5 nm for the AB@ZIF-8 composite. The reduction of the crystallite size occurs due to the effect of the borane present during the formation of ZIF-8. This might be explained by the

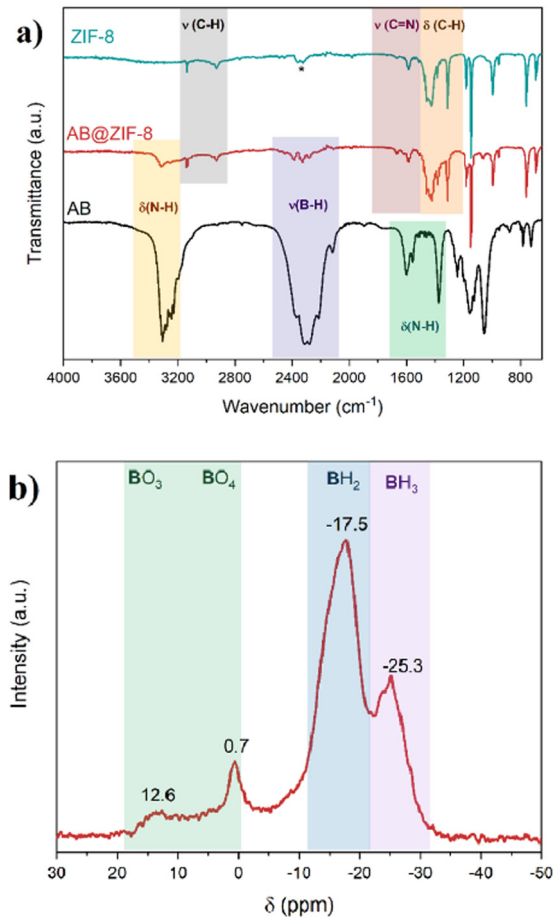

Fig. 2 (a) IR spectra of ZIF-8, AB@ZIF-8 and AB. The relevant vibrational modes are indicated in the coloured rectangles. (b) ^{11}B MAS NMR spectrum of AB@ZIF-8. The chemical shifts in ppm and the relevant chemical environments in the coloured rectangles are indicated.

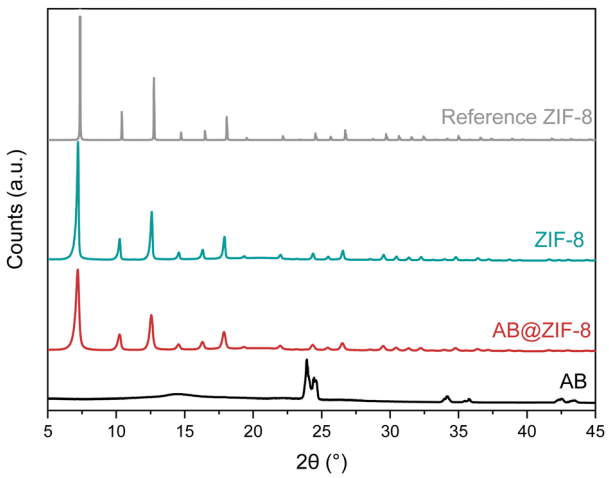

Fig. 3 PXRD patterns of the synthesized ZIF-8 and the AB@ZIF-8 composite. For comparison, the patterns of AB and reported ZIF-8 are also presented.

interactions of the AB molecules with the precursors, which would limit the growth of the ZIF-8 crystals.

Thermal analyses were carried out for pristine ZIF-8 and AB@ZIF-8. Pristine ZIF-8 shows stability up to 220 °C, beyond which decomposition initiates. At 400 °C, approximately 2 wt% of the original weight is lost (Fig. 4).

In the case of AB@ZIF-8, a distinct behavior is observed: decomposition starts at 40 °C, with approximately 1.5 wt% loss at 200 °C and about 4 wt% 400 °C. The DSC curve of the AB@ZIF-8 composite presents an exothermic event at 92 °C, which indicates the release of H_2 from AB (Fig. S5, ESI†). It is known that under constant heating, bulk AB melts before releasing H_2, and then it starts to decompose at around 100 °C so the first dehydrogenation event takes place at 110–120 °C.[35] With respect to AB@ZIF-8, there is no melting of AB (evidenced by the lack of an endothermic event); AB decomposes from 40 °C, and the main release of H_2 occurs at 92 °C. All of these characteristics are typical of nanoconfined AB, and it has been observed in similar systems (AB confined in ZIF-8).[21]

AB@ZIF-8 was analyzed by XPS, and the resulting spectra are shown in Fig. 5 (the survey scan is shown in Fig. S6, ESI†). The B 1s spectrum was deconvoluted into two signals. The first one is centered at 189.1 eV, and it corresponds to the B–H bond of AB. We do not discard the possible contribution of a boride species (B–Zn) to this signal, as metal borides appear between 187 and 189 eV.[36] The second peak at 191.4 eV is related to B–N and B–O bonds.[37,38] This is in good agreement with the ^{11}B MAS NMR spectrum of the sample, where the borate environment was detected. The N 1s spectrum was deconvoluted in three peaks centered at 400.0, 398.7 and 397.9 eV. The first one corresponds to the nitrogen in the imidazole group N═C, the second to the N–B bond of AB, and the third one corresponds to the N–H bond.[36,39–41] In the case of the C 1s spectrum, the signal at 286.1 eV indicates the carbon linked to the imidazole nitrogen, and the one at 287.3 eV is due to carbonyl groups or carbonates that can accumulate on the surface of the material when it is put in air.[39,40] Regarding the Zn 2p spectrum, it shows the two characteristic peaks observed in pristine ZIF-8 centered at 1021.2 and 1044.3 eV, which correspond to Zn $2p_{3/2}$ and Zn

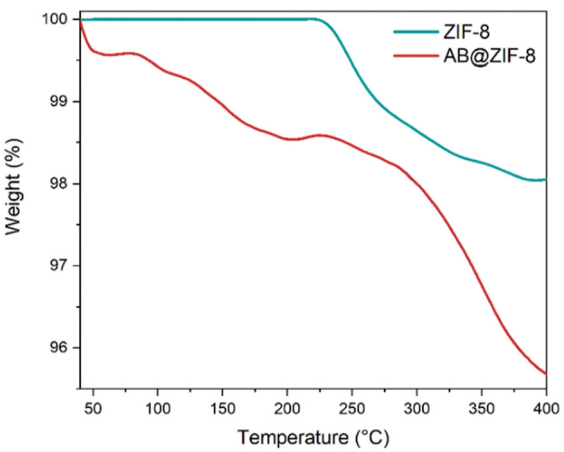

Fig. 4 Thermogravimetric analyses of pristine ZIF-8 and AB@ZIF-8.

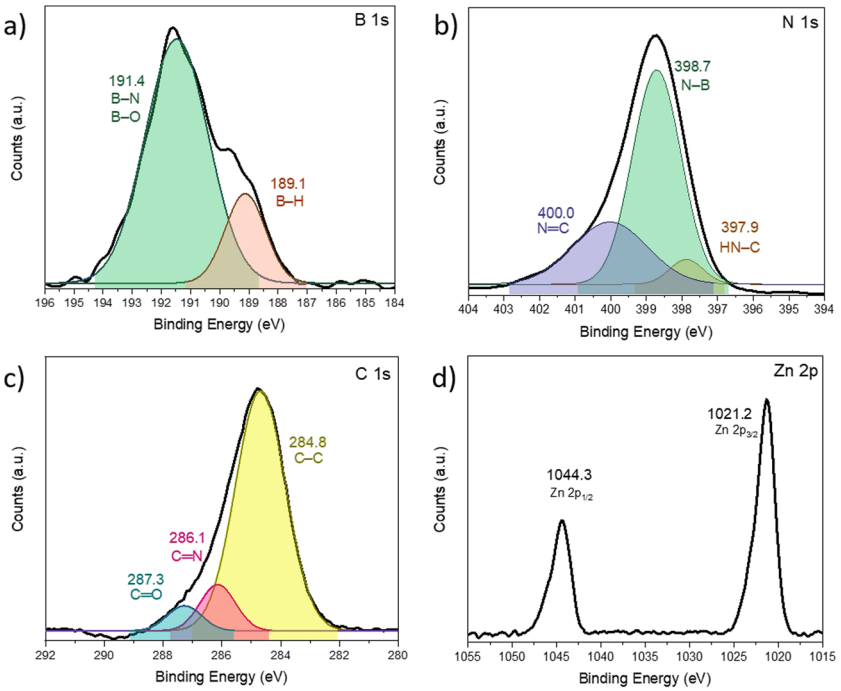

Fig. 5 XPS spectra of AB@ZIF-8 for (a) B 1s, (b) N 1s, (c) C 1s, and (d) Zn 2p. The deconvolution was made with a Gaussian fit. The binding energies in eV and the associated bonds are indicated.

$2p_{1/2}$ respectively.[42,43] The binding energy distance between these peaks is 23.1 eV, indicating a 2+ state of the zinc atom.[44]

3.3 BN@C

The AB@ZIF-8 sample was pyrolyzed under N_2 at 800 °C, in order to obtain a structure composed of B, N and C (BN@C). ICP-MS and elemental analyses were performed to provide a better overview of the sample composition, obtaining the following results: B (9.5 wt%), N (21.2 wt%) C (50.8 wt%), Zn (11.8 wt%) and H (2.9 wt%). The presence of B–O bonds was detected by ^{11}B MAS NMR and XPS in the AB@ZIF-8 composite, and some oxygen atoms might have been present during pyrolysis. Therefore, the rest of this compound is attributed to oxygen (3.8% wt). Taking into account the atomic fractions of each element, the formula of BN@C is thus $C_{1.00}B_{0.20}N_{0.35}$-$H_{0.68}O_{0.05}Zn_{0.04}$. For comparison, the weight percentages calculated by XPS are 3.8 wt% (B), 20.5 wt% (N), 51.1 wt% (C), and 15.9 wt% (Zn). The results are consistent, except for the boron, which presents a lower value by XPS. This can be explained by the possible migration of boron atoms during the analyses due to the X-ray beam.[45] Another plausible reason to explain this is that XPS only analyzes the surface of the material and it does not takes into account the bulk material.

The BN@C composite was analyzed by Raman spectroscopy (Fig. 6a). Two bands can be observed in the spectrum at 1340 and 1585 cm^{-1} (bands D and G, respectively). The G band originates from the E_{2g} vibrational mode and is related to the motion between sp^2 carbon atoms.[46] The D band, which stands

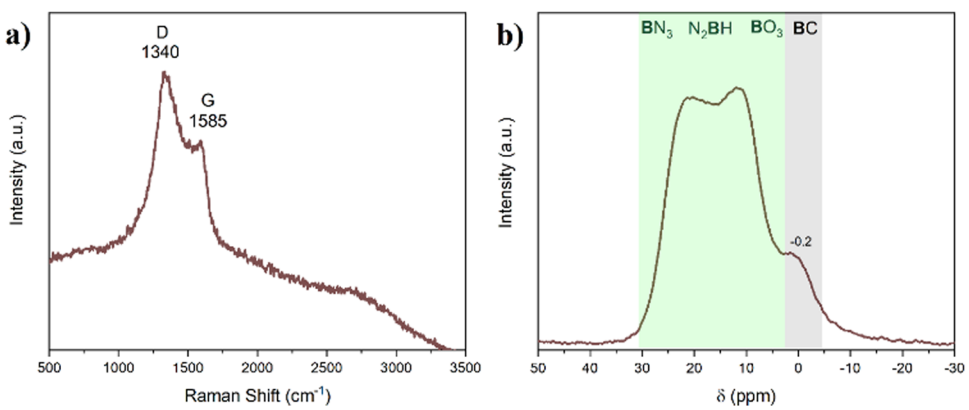

Fig. 6 (a) Raman spectrum and (b) 11B MAS NMR spectrum of the BN@C composite. The Raman shift in cm^{-1} and the chemical shifts in ppm are indicated. The chemical environments are highlighted by the coloured rectangles.

for the ''defect'', is originated from the A_{1g} breathing mode of the carbon rings.[47] This band also increases and broadens with the presence of defects. The intensity of the D band in the sample is greater than that of the G band, indicating a disordered sample with defects.

BN@C is amorphous (Fig. S7, ESI†). It exhibits two broad bands between 25–30° and 40–45°. The presence of these signals is the characteristic from amorphous carbon, but also from amorphous BN with a weak stacking of the layers.[48]

BN@C was analyzed by ^{11}B MAS NMR (Fig. 6b). In comparison with AB@ZIF-8, all the tetracoordinated boron environments have disappeared. A double-horned broad band has appeared between 0 and 30 ppm. The environments between 20 and 30 ppm are typical of $\mathbf{B}N_3$ and $N_2\mathbf{B}H$ environments, indicating the formation of BN.[49] It is likely that other signals are contributing to the intensity of the band, such as the $\mathbf{B}O_3$ environments (around 15 ppm) present in the AB@ZIF-8 sample before pyrolysis. A new band centered at −0.2 ppm appeared and it indicates the presence of a **B**C environment.[18] This is a first indication that B–C bonds have been formed during the pyrolysis of the sample.

BN@C was analyzed by XPS (Fig. 7 and Fig. S8, ESI†). The B 1s spectrum consists of two signals centered at 190.3 and 191.5 eV. The first one is assigned to the B–N bond of BN.[50] The second one is typically from B–O bonds. However, in this case, it is likely that the B atom is also bonded either to a N atom or to a C atom (N–B–O or C–B–O). The N 1s spectrum was deconvoluted into four signals and they were assigned based on the literature of similar materials.[51–53] The first one, centered at 398.1 eV, is assigned to the N–B bond of BN, but also to pyridinic N (a nitrogen on the edge of the carbon structure linking two carbon atoms). The signals at 399.3, 400.1 and 402 eV are assigned to pyrrolic N (a nitrogen on the edge of the graphitic structure linking two carbon atoms and a hydrogen atom), graphitic N (a N atom in the middle of the graphitic structure linked to three C atoms), and oxidized N (a N atom on the edge of the carbon structure linking two carbon atoms and an oxygen atom), respectively. The C 1s spectrum was deconvoluted into several signals, and they were assigned.[54–56] The peak at 284.4 eV is originated by the C–C bond. The peaks at 285.2 and 286.6 eV are related to C–N and C═N bonds, respectively. The signal present at 285.7 eV has been ascribed to the C–B bond, which is in agreement with the B 1s XPS and the ^{11}B MAS NMR spectra of the material. This suggests that during the pyrolysis process, bonds between C and B are formed. Finally, the Zn 2p spectrum does not present changes with respect to AB@ZIF-8, which indicates that Zn is still in a 2+ state (most likely as ZnO, but we do not discard the possibility that Zn is stabilized within the structure).

With the preceding results, we can now analyse the nature of the BN@C composite. AB was entrapped within the porosity of ZIF-8 and subsequently underwent pyrolysis. TEM images

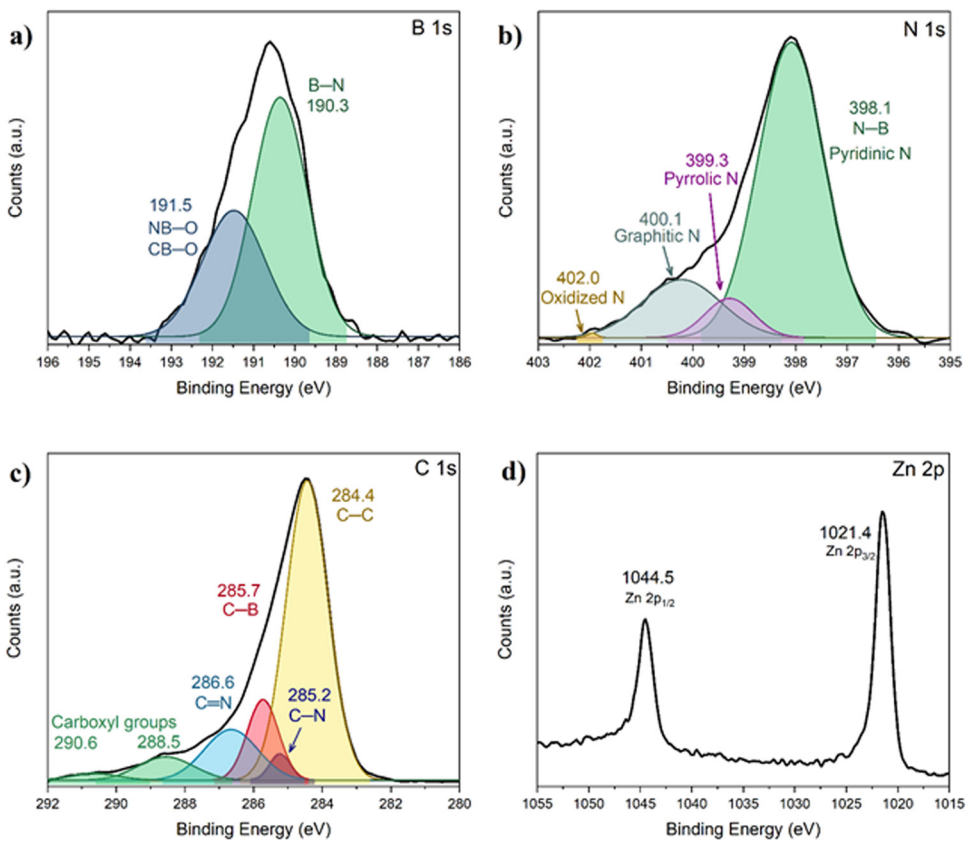

Fig. 7 XPS spectra of BN@C for (a) B 1s, (b) N 1s, (c) C 1s, and (d) Zn 2p. The deconvolution was made with a Gaussian fit. The binding energies in eV and the associated bonds are indicated.

Table 2 CO_2 uptake capacity of the samples under 1.5 bar and at 30 °C

	CO_2 uptake per mass unit			CO_2 uptake per specific surface area unit		
Sample	$cm^3\ g^{-1}$	$mg\ g^{-1}$	$mmol\ g^{-1}$	$cm^3\ m^{-2}$	$mg\ m^{-2}$	$mmol\ m^{-2}$
ZIF-8	16.1	32	0.7	0.01	0.02	0.56×10^{-3}
C800	42.3	83.2	1.9	0.06	0.12	2.7×10^{-3}
BN@C	43.4	85.5	1.9	0.77	1.52	34×10^{-3}

revealed that BN@C retained the structure of ZIF-8, suggesting that BN was formed within the material. This observation may account for the discrepancy in elemental boron quantification between XPS and ICP-OES analyses. As XPS analyses a few nanometers of the surface, it is possible that a significant portion of boron resides within the structure.

Analyses of Raman spectroscopy, elemental composition, and XPS C 1s all indicated a substantial amount of carbon with various bonding types (C–C, C–B, and C═N). Both ^{11}B MAS NMR and XPS B 1s analyses confirmed the formation of boron nitride and the existence of B–C bonds. XPS N 1s analysis corroborates the formation of BN and shows diverse environments within the carbon structure (pyrrolic, graphitic or oxidized nitrogen). In summary, it is plausible that BN@C is a composite comprising graphite/graphene (doped with nitrogen), boron nitride and regions of boron carbon nitride.

3.4 CO_2 adsorption experiments

The CO_2 sorption capacity of the BN@C composite was evaluated under nearly room conditions. For comparison, we also assessed the sorption capacity of pristine ZIF-8 and C800.

As shown in Table 1, the SSAs of ZIF-8, C800 and BN@C are 1281, 658 and 56 $m^2\ g^{-1}$, respectively. The samples were degassed before the analysis and then they were exposed to a CO_2 atmosphere at a constant temperature. The estimated adsorption capacity is presented in Table 2. The pristine ZIF-8 was able to capture 0.72 mmol $CO_2\ g^{-1}$ at 1.5 bar CO_2 and 30 °C. This value is in line with the ones reported in the literature. For example, one study reported an adsorption of 0.65 mmol $CO_2\ g^{-1}$ at 1 bar and 30 °C by ZIF-8,[57] whereas another one reported a value of 0.8 mmol $CO_2\ g^{-1}$ at 1 bar CO_2 and 25 °C.[58]

C800 and BN@C exhibited enhanced CO_2 adsorption. Under the same conditions, C800 adsorbed 1.89 mmol $CO_2\ g^{-1}$, and BN@C at 1.94 mmol g^{-1}. At 0 °C and 45 °C, BN@C exhibited CO_2 adsorption capacities of 2.26 mmol $CO_2\ g^{-1}$ and 1.48 mmol $CO_2\ g^{-1}$, respectively (Table S1, ESI†). Using these data, we calculated the isosteric enthalpy of adsorption of BN@C using the Clausius–Clapeyron equation resulting in a value of -12 ± 4 kJ mol^{-1}. This suggests that the adsorption mechanism involves only physical interactions, as values of $\Delta H_{ads} > -50$ kJ mol^{-1} are typical for physisorption (Fig. S9, ESI†).

Although the CO_2 uptake per mass unit of BN@C is similar to that of C800, the scenario changes when considering the specific surface area. Compared to ZIF-8, the CO_2 uptake per surface area unit of BN@C is more than 60 times higher (0.56×10^{-3} mmol m^{-2} *vs.* 34×10^{-3} mmol m^{-2}), and compared to C800, it is more than 10 times higher (2.7×10^{-3} mmol m^{-2} *vs.* 34×10^{-3} mmol m^{-2}). The specific surface areas of ZIF-8 and C800 are 22 times and 10 times higher, respectively, than that of BN@C. Despite this, BN@C adsorbs more CO_2 per area unit, suggesting that the presence of active sites for CO_2 adsorption has a strong impact on the adsorption properties of the material.

Given the nature of BN@C, different active sites may exist within the composite structure. Theoretical calculations have identified strong adsorption sites in boron carbon nitride materials:[66] (i) weakly negative charged nitrogen atoms bonded with at least one carbon atom; (ii) boron atoms bonded with three nitrogen atoms, attracting the negatively charged oxygen of the CO_2 molecules; and (iii) carbon bonded with two nitrogen atoms, exhibiting a slightly positive charge that can attract CO_2 molecules. Another theoretical study suggests that CO_2 molecules tend to adsorb on B–C sites, although they also adsorb on other sites (C–C, B–N, and C–N).[63] Yet, another study proposes that boron vacancies within the boron nitride structure can enhance CO_2 sorption.[67] Experimental observations support some of these points. It has been reported that N-doped graphene enhances CO_2 adsorption capacity at different temperatures compared to pristine graphene, due to the presence of local Lewis basic sites, such as the different nitrogen species present in the structure (*e.g.* pyridinic and pyrrolic).[68,69] The nitrogen atom bonded to a boron atom was also found to be an active site for CO_2 adsorption.[70]

Table 3 CO_2 uptake by different BN- and ZIF-8-based materials

Material	T (°C)	P (bar)	SSA ($m^2\ g^{-1}$)	CO_2 uptake		Ref.
				$mmol\ g^{-1}$	$mmol\ m^{-2}$	
AB pyrolyzed at 800 °C	30	1.5	—	1.46	—	23
BN@C	30	1.5	56	1.94	34×10^{-3}	This work
Porous h-BN	25	1	212	0.86	4×10^{-3}	59
Porous h-BN doped with carbon	25	1	727	3.91	5×10^{-3}	18
NH_3-treated carbon derived from ZIF-8	20	1	805	1.49	81×10^{-3}	60
ZIF-8 modified with NH_3	25	1	972	0.56	0.5×10^{-3}	61
Flower-like BN nanosheets	25	1	1114	0.85	0.7×10^{-3}	62
Ordered mesoporous BCN	25	1	1166	1.64	1.4×10^{-3}	63
ZIF-8 modified with PEI	30	1	1312	0.92	0.7×10^{-3}	57
Porous BN	25	1	1585	1.22	0.7×10^{-3}	64
BCN conjugated nanoporous carbon	25	1	2108	2.38	1.1×10^{-3}	65

As evidenced by the characterization results, our BN@C likely contains numerous active sites for CO_2 adsorption (as those mentioned above). This may thus explain the high capture capacity in terms of the specific surface area.

When compared to similar materials under similar conditions, the BN@C composite shows an improvement in CO_2 capture capacity (Table 3). Porous materials based on B, N and C have a superior adsorption capacity per mass unit, but when it is compared in terms of the SSA, our material presents a higher capacity. It is thus clear that to improve the overall CO_2 adsorption, the synthesis of porous boron-, carbon-, and nitrogen-based materials is desirable.

4. Conclusions

In this study, a composite made of carbon and boron nitride was obtained *via* the confinement of AB into a MOF, ZIF-8. In the first step, we trapped AB inside the structure of ZIF-8 through a novel one-pot synthesis method that we developed. Through different characterization techniques, the successful infiltration of AB was demonstrated. In the second step, the material was pyrolyzed at 800 °C. The pure ZIF-8 showed a BET specific surface area of 1281 $m^2\ g^{-1}$, whereas for BN@C, it measured 56 $m^2\ g^{-1}$. The decrease in the specific surface area can be attributed to the inclusion of BN within the pores. The pyrolysis process led to a composite made of graphene/graphite, boron nitride and boron carbon nitride.

The CO_2 adsorption capacity of the composite was assessed. When considering the uptake per mass unit, the BN@C composite exhibited more than double the CO_2 adsorption of pristine ZIF-8 (1.94 *vs.* 0.72 mmol g^{-1}). In comparison to ZIF-8 treated at 800 °C, the improvement was minimal. However, when evaluating the uptake per specific surface area unit, BN@C demonstrated a CO_2 adsorption approximately 60 times greater than that of ZIF-8 (34×10^{-3} *vs.* 0.56×10^{-3} mmol m^{-2}). Compared to ZIF-8 treated at 800 °C, the uptake was increased by over 10 times (34×10^{-3} *vs.* 2.7×10^{-34} mmol m^{-2}).

Despite the lower specific surface area of BN@C, the composite displayed a higher capacity for CO_2 per specific surface area unit compared to similar materials. This suggests the presence of various defects and other active sites for CO_2 adsorption (*e.g.* polarized B–C, B–N and C–N bonds), enhancing gas capture. We conclude that a high density of active sites is more important than a large specific surface area, at least under the conditions applied in this study. Additionally, it is plausible that by controlling the B/C ratio, and thus the number of active sites, one can tailor the adsorption properties of the structures. Experiments are currently underway to investigate these points.

Our primary goal was to enhance the adsorption capacity of BN structures by incorporating carbon, and we successfully achieved this objective. It is much likely that the design of porous materials based on boron, nitrogen and carbon might improve the CO_2 adsorption, which open new perspectives for boron-based materials.

Conflicts of interest

There are no conflicts to declare.

Acknowledgements

The authors want to acknowledge Christelle Miqueu for the density measurements of the samples, Eddy Petit for the Raman spectroscopy analyses, and Rimeh Mighri and Johan Alauzun for the elemental analyses.

Notes and references

1 Q. He and B. R. Silliman, *Curr. Biol.*, 2019, **29**, R1021–R1035.
2 N. S. Sifat and Y. Haseli, *Energies*, 2019, **12**, 4143.
3 International Energy Agency, CCUS in clean energy transitions.
4 F. Marocco Stuardi, F. MacPherson and J. Leclaire, *Curr. Opin. Green Sustainable Chem.*, 2019, **16**, 71–76.
5 S. Zhang, C. Chen and W.-S. Ahn, *Curr. Opin. Green Sustainable Chem.*, 2019, **16**, 26–32.
6 D. Saha and M. J. Kienbaum, *Microporous Mesoporous Mater.*, 2019, **287**, 29–55.
7 G. Gómez-Pozuelo, E. S. Sanz-Pérez, A. Arencibia, P. Pizarro, R. Sanz and D. P. Serrano, *Microporous Mesoporous Mater.*, 2019, **282**, 38–47.
8 T. Ghanbari, F. Abnisa and W. M. A. Wan Daud, *Sci. Total Environ*, 2020, **707**, 135090.
9 P. Bhanja, A. Modak and A. Bhaumik, *ChemCatChem*, 2019, **11**, 244–257.
10 J. Bai, J. Huang, Q. Jiang, W. Jiang, M. Demir, M. Kilic, B. N. Altay, L. Wang and X. Hu, *Colloids Surf., A*, 2023, **674**, 131916.
11 Y. Sang, Y. Cao, L. Wang, W. Yan, T. Chen, J. Huang and Y.-N. Liu, *J. Colloid Interface Sci.*, 2021, **587**, 121–130.
12 S. Roy, X. Zhang, A. B. Puthirath, A. Meiyazhagan, S. Bhattacharyya, M. M. Rahman, G. Babu, S. Susarla, S. K. Saju, M. K. Tran, L. M. Sassi, M. A. S. R. Saadi, J. Lai, O. Sahin, S. M. Sajadi, B. Dharmarajan, D. Salpekar, N. Chakingal, A. Baburaj, X. Shuai, A. Adumbumkulath, K. A. Miller, J. M. Gayle, A. Ajnsztajn, T. Prasankumar, V. V. J. Harikrishnan, V. Ojha, H. Kannan, A. Z. Khater, Z. Zhu, S. A. Iyengar, P. A. da S. Autreto, E. F. Oliveira, G. Gao, A. G. Birdwell, M. R. Neupane, T. G. Ivanov, J. Taha-Tijerina, R. M. Yadav, S. Arepalli, R. Vajtai and P. M. Ajayan, *Adv. Mater.*, 2021, **33**, 2101589.
13 S. Marchesini, A. Regoutz, D. Payne and C. Petit, *Microporous Mesoporous Mater.*, 2017, **243**, 154–163.
14 H. Jiang, L. Ma, Q. Yang, Z. Tang, X. Song, H. Zeng and C. Zhi, *Solid State Commun.*, 2019, **294**, 1–5.
15 Z. Zhang, Z. P. Cano, D. Luo, H. Dou, A. Yu and Z. Chen, *J. Mater. Chem. A*, 2019, **7**, 20985–21003.
16 J. Gou, C. Liu, J. Lin, C. Yu, Y. Fang, Z. Liu, Z. Guo, C. Tang and Y. Huang, *Ceram. Int.*, 2022, **48**, 11636–11643.

17 J. Liang, Q. Song, J. Lin, G. Li, Y. Fang, Z. Guo, Y. Huang, C.-S. Lee and C. Tang, *ACS Sustainable Chem. Eng.*, 2020, **8**, 7454–7462.
18 S. Chen, P. Li, S. Xu, X. Pan, Q. Fu and X. Bao, *J. Mater. Chem. A*, 2018, **6**, 1832–1839.
19 D. N. Ta, H. K. D. Nguyen, B. X. Trinh, Q. T. N. Le, H. N. Ta and H. T. Nguyen, *Can. J. Chem. Eng.*, 2018, **96**, 1518–1531.
20 Z. Li, G. Zhu, G. Lu, S. Qiu and X. Yao, *J. Am. Chem. Soc.*, 2010, **132**, 1490–1491.
21 R. Q. Zhong, R. Q. Zou, T. Nakagawa, M. Janicke, T. A. Semelsberger, A. K. Burrell and R. E. Del Sesto, *Inorg. Chem.*, 2012, **51**, 2728–2730.
22 G. Srinivas, W. Travis, J. Ford, H. Wu, Z. X. Guo and T. Yildirim, *J. Mater. Chem. A*, 2013, **1**, 4167–4172.
23 C. A. Castilla-Martinez, R. Mighri, C. Charmette, J. Cartier and U. B. Demirci, *Energy Technol.*, 2023, **11**, 2201521.
24 G. Moussa, S. Bernard, U. B. Demirci, R. Chiriac, P. Miele and D. Lyon, *Int. J. Hydrogen Energy*, 2012, **37**, 13437–13445.
25 C. Young, R. R. Salunkhe, J. Tang, C.-C. C. Hu, M. Shahabuddin, E. Yanmaz, M. S. A. Hossain, J. H. Kim and Y. Yamauchi, *Phys. Chem. Chem. Phys.*, 2016, **18**, 29308–29315.
26 H. Kaur, G. C. Mohanta, V. Gupta, D. Kukkar and S. Tyagi, *J. Drug Delivery Sci. Technol.*, 2017, **41**, 106–112.
27 N. Li, L. Zhou, X. Jin, G. Owens and Z. Chen, *J. Hazard. Mater.*, 2019, **366**, 563–572.
28 M. He, J. Yao, Q. Liu, K. Wang, F. Chen and H. Wang, *Microporous Mesoporous Mater.*, 2014, **184**, 55–60.
29 U. B. Demirci, *Int. J. Hydrogen Energy*, 2017, **42**, 9978–10013.
30 Z. Cao, L. Ouyang, M. Felderhoff and M. Zhu, *RSC Adv.*, 2020, **10**, 19027–19033.
31 M. Bowden, D. J. Heldebrant, A. Karkamkar, T. Proffen, G. K. Schenter and T. Autrey, *Chem. Commun.*, 2010, **46**, 8564–8566.
32 X. Si, L. Sun, F. Xu, C. Jiao, F. Li and S. Liu, *Int. J. Hydrogen Energy*, 2011, **36**, 6698–6704.
33 G. Srinivas, J. Ford, W. Zhou and T. Yildirim, *Int. J. Hydrogen Energy*, 2011, **37**, 3633–3638.
34 K. S. Park, Z. Ni, A. P. Côté, J. Y. Choi, R. Huang, F. J. Uribe-Romo, H. K. Chae, M. O'Keeffe and O. M. Yaghi, *Proc. Natl. Acad. Sci. U. S. A.*, 2006, **103**, 10186–10191.
35 S. Frueh, R. Kellett, C. Mallery, T. Molter, W. S. Willis, C. King'Ondu and S. L. Suib, *Inorg. Chem.*, 2011, **50**, 783–792.
36 A. V. Naumkin, A. Kraust-Vass, S. W. Gaarenstroom and C. J. Powell, NIST XPS Database, **https://srdata.nist.gov/xps/Default.aspx**.
37 S. K. Young, J. Park, C. C. Hyun, P. A. Jae, Q. H. Jin and S. K. Hong, *J. Am. Chem. Soc.*, 2007, **129**, 1705–1716.
38 Y. Wei, P. Wu, J. Luo, L. Dai, H. Li, M. Zhang, L. Chen, L. Wang, W. Zhu and H. Li, *Microporous Mesoporous Mater.*, 2020, **293**, 109788.
39 S. Bhattacharyya, S. H. Pang, M. R. Dutzer, R. P. Lively, K. S. Walton, D. S. Sholl and S. Nair, *J. Phys. Chem. C*, 2016, **120**, 27221–27229.
40 F. Tian, A. M. Cerro, A. M. Mosier, H. K. Wayment-Steele, R. S. Shine, A. Park, E. R. Webster, L. E. Johnson, M. S. Johal and L. Benz, *J. Phys. Chem. C*, 2014, **118**, 14449–14456.
41 CNRS, La surface XPS database, **https://www.lasurface.com/database/index.php#**.
42 H. Chen, L. Wang, J. Yang and R. T. Yang, *J. Phys. Chem. C*, 2013, **117**, 7565–7576.
43 M. Jian, B. Liu, G. Zhang, R. Liu and X. Zhang, *Colloids Surf., A*, 2015, **465**, 67–76.
44 J. Liu, J. He, L. Wang, R. Li, P. Chen, X. Rao, L. Deng, L. Rong and J. Lei, *Sci. Rep.*, 2016, **6**, 1–11.
45 J.-F. Ying, R. Ji, C. C. Wang, S. Ter Lim, H. Xie and E. F. Gerard, *J. Mater. Eng. Perform.*, 2014, **23**, 2795–2800.
46 T. Xing, L. H. Li, L. Hou, X. Hu, S. Zhou, R. Peter, M. Petravic and Y. Chen, *Carbon*, 2013, **57**, 515–519.
47 A. Merlen, J. Buijnsters and C. Pardanaud, *Coatings*, 2017, **7**, 153.
48 W. Lei, D. Liu and Y. Chen, *Adv. Mater. Interfaces*, 2015, **2**, 2–7.
49 C. Gervais, E. Framery, C. Duriez, J. Maquet, M. Vaultier and F. Babonneau, *J. Eur. Ceram. Soc.*, 2005, **25**, 129–135.
50 Q. Weng, L. Zeng, Z. Chen, Y. Han, K. Jiang, Y. Bando and D. Golberg, *Adv. Funct. Mater.*, 2021, **31**, 2007381.
51 M. Shang, X. Zhang, J. Zhang, J. Sun, X. Zhao, S. Yu, X. Liu, B. Liu and X. Yi, *Carbohydr. Polym.*, 2021, **262**, 117966.
52 Y. Xiao, H. Yang, X. Bu and P. Feng, *Carbon*, 2021, **176**, 421–430.
53 X. Ma, L. Li, S. Wang, M. Lu, H. Li, W. Ma and T. C. Keener, *Appl. Surf. Sci.*, 2016, **369**, 390–397.
54 M. Xing, W. Fang, X. Yang, B. Tian and J. Zhang, *Chem. Commun.*, 2014, **50**, 6637–6640.
55 J. Xiong, W. Zhu, H. Li, L. Yang, Y. Chao, P. Wu, S. Xun, W. Jiang, M. Zhang and H. Li, *J. Mater. Chem. A*, 2015, **3**, 12738–12747.
56 M. Jiang, X. Cao, D. Zhu, Y. Duan and J. Zhang, *Electrochim. Acta*, 2016, **196**, 699–707.
57 J. Pokhrel, N. Bhoria, S. Anastasiou, T. Tsoufis, D. Gournis, G. Romanos and G. N. Karanikolos, *Microporous Mesoporous Mater.*, 2018, **267**, 53–67.
58 J. McEwen, J.-D. Hayman and A. Ozgur Yazaydin, *Chem. Phys.*, 2013, **412**, 72–76.
59 S. Li, X. Zeng, H. Chen, W. Fang, X. He, W. Li, Z. Huang and L. Zhao, *Ceram. Int.*, 2020, **46**, 27627–27633.
60 X. Ma, L. Li, S. Wang, M. Lu, H. Li, W. Ma and T. C. Keener, *Appl. Surf. Sci.*, 2016, **369**, 390–397.
61 Z. Zhang, S. Xian, H. Xi, H. Wang and Z. Li, *Chem. Eng. Sci.*, 2011, **66**, 4878–4888.
62 C. Yang, J. Wang, Y. Chen, D. Liu, S. Huang and W. Lei, *Nanoscale*, 2018, **10**, 10979–10985.
63 C. Sathish, G. Kothandam, P. Selvarajan, Z. Lei, J. Lee, J. Qu, A. H. Al-Muhtaseb, X. Yu, M. B. H. Breese, R. Zheng, J. Yi and A. Vinu, *Adv. Sci.*, 2022, **9**, 2105603.
64 R. Shankar, M. Sachs, L. Francàs, D. Lubert-Perquel, G. Kerherve, A. Regoutz and C. Petit, *J. Mater. Chem. A*, 2019, **7**, 23931–23940.
65 R. Bahadur, G. Singh, M. Li, D. Chu, J. Yi, A. Karakoti and A. Vinu, *Chem. Eng. J.*, 2023, **460**, 141793.
66 K. Raidongia, A. Nag, K. P. S. S. Hembram, U. V. Waghmare, R. Datta and C. N. R. Rao, *Chem. – Eur. J.*, 2010, **16**, 149–157.
67 Y. Jiao, A. Du, Z. Zhu, V. Rudolph, G. Q. Lu and S. C. Smith, *Catal. Today*, 2011, **175**, 271–275.

68 P. Tamilarasan and S. Ramaprabhu, *J. Appl. Phys.*, 2015, **117**, 144301.
69 L. Ouyang, J. Xiao, H. Jiang and S. Yuan, *Molecules*, 2021, **26**, 5293.
70 M. K. Hussien, A. Sabbah, M. Qorbani, M. H. Elsayed, S. Quadir, P. Raghunath, D.-L. M. Tzou, S.-C. Haw, H.-H. Chou, N. Q. Thang, M.-C. Lin, L.-C. Chen and K.-H. Chen, *Mater. Today Sustain.*, 2023, **22**, 100359.

